Earth and Planetary Science Letters 578 (2022) 117295

Contents lists available at ScienceDirect

Earth and Planetary Science Letters

www.elsevier.com/locate/epsl

Spectral amplification of ground motion linked to resonance of large-scale mountain landforms

Samuel Weber [a,b,c,*], Jan Beutel [d,e], Mauro Häusler [f], Paul R. Geimer [g], Donat Fäh [f], Jeffrey R. Moore [g]

[a] Chair of Landslide Research Group, Technical University of Munich, Munich, Germany
[b] WSL Institute for Snow and Avalanche Research SLF, Davos Dorf, Switzerland
[c] Climate Change, Extremes and Natural Hazards in Alpine Regions Research Center CERC, Davos Dorf, Switzerland
[d] Computer Engineering and Networks Laboratory, ETH Zurich, Zurich, Switzerland
[e] Department of Computer Science, University of Innsbruck, Austria
[f] Swiss Seismological Service, ETH Zurich, Zurich, Switzerland
[g] Department of Geology & Geophysics, University of Utah, Salt Lake City, UT, USA

ARTICLE INFO

Article history:
Received 9 June 2021
Received in revised form 7 November 2021
Accepted 10 November 2021
Available online 22 December 2021
Editor: H. Thybo

Keywords:
ambient vibration
modal analysis
topographic seismic amplification
eigenfrequency modeling
Alpine mountains

ABSTRACT

Amplification of seismic energy in steep topography plays an important role controlling the location of earthquake-induced landslides. Alpine mountains represent extreme topography, therefore large amplification may be anticipated, however suitable data needed to probe the limits of topographic effects in these demanding locations are rare. Here we present new ambient vibration data from seismic stations on the summit and ridge of one of the tallest freestanding mountains in the Swiss Alps – the Matterhorn – comparing these to a nearby local reference. Results show elevated spectral power at mountain stations between 0.4 and 1 Hz, and directional site-to-reference spectral amplitude ratios up to 14, which we attribute in part to topographic resonance. We used ambient vibration modal analysis and numerical eigenfrequency modeling to identify the fundamental mode of the Matterhorn at 0.42 Hz, as well as evidence for a second, mutually-perpendicular mode at a similar frequency. We identified high modal damping ratios of ~20% for these modes, which we ascribe to radiative energy loss. A short campaign measurement at another mountain of comparable shape but smaller scale showed similar modal properties with a higher fundamental frequency of 1.8 Hz and peak spectral ratios of 6. Tracking of resonant frequencies over one year at the Matterhorn revealed no measurable seasonal variations related to near-surface environmental changes (e.g. temperature, ice). Our results demonstrate large spectral amplifications linked to resonance of high-relief mountain landforms, which is likely to be a widespread effect making such areas more prone to co-seismic rock damage and landslides.

1. Introduction

Topographic amplification of seismic energy arises due to resonance and wave focusing in steep topography, resulting in amplified ground motions at slope crests and convex breaks as compared to adjacent valley-bottom reference sites (Boore, 1972; Davis and West, 1973; Çelebi, 1987; Meunier et al., 2008). This phenomenon is distinguished from localized site effects resulting from near-surface soil stratigraphy or weathered rock shear-wave velocity contrasts, as well as the presence of rock fractures (Borcherdt, 1970; Havenith et al., 2002; Moore et al., 2011; Burjánek et al., 2012; Häusler et al., 2019). While the latter are commonly implicated in generating large spectral amplifications (factors up to and greater than ~10), as measured using standard site-to-reference spectral ratios, topographic effects predicted from simulations are generally smaller, with peak amplification <2 in most cases (e.g. Ashford et al., 1997; Paolucci, 2002; Burjánek et al., 2014; Gischig et al., 2015). Nonetheless, topographic amplification is widespread and has been shown to play an important role affecting the locations of earthquake-induced damage and the distribution of earthquake-triggered landslides (Çelebi, 1987; Harp and Jibson, 2002; Havenith et al., 2003; Sepúlveda et al., 2005; Hough et al., 2010).

Incoming seismic energy can excite resonance of topographic landforms with similar wavelength, resulting in amplified and polarized ground motion (Boore, 1972; Panzera et al., 2011; Massa

* Corresponding author at: WSL Institute for Snow and Avalanche Research SLF, Davos Dorf, Switzerland.
E-mail address: samuel.weber@slf.ch (S. Weber).

https://doi.org/10.1016/j.epsl.2021.117295

et al., 2014; Stolte et al., 2017; Moore et al., 2019). Thus attributes of topographic amplification depend to the first order on the scale and shape of topography, which controls the frequencies and modal vectors of the excited resonant modes. Past experimental studies have measured topographic effects in a variety of settings, from relatively small (∼15 m) to large (∼700 m high) ridges and hilltops, showing strong polarization of ground motion and peak spectral amplification values around 2 to 10 (e.g. Pedersen et al., 1994; Spudich et al., 1996; LeBrun et al., 1999; Massa et al., 2014; Stolte et al., 2017). However, distinguishing topographic resonance effects from commingled localized site effects often complicates interpretation of these data (Burjánek et al., 2014; Kleinbrod et al., 2019; Rault et al., 2020). Mountains, and especially the large freestanding massifs of the European Alps, on the other hand, represent extreme topography and may thus exhibit larger topographic amplification than features with less relief. However, suitable broadband seismic data from these locations are rare, in part due to difficult and often dangerous site access as well as limited measurement locations, and thus data needed to probe the range of topographic amplification remain limited.

Dissipation of seismic energy with time is described by modal damping ratios (Chopra, 2012a; here referred to as damping). Damping results from thermal and viscoelastic energy dissipation (material damping) as well as geometric effects and material contrasts (radiation damping), but distinguishing the sources of damping is rarely possible (Çelebi, 1996; Ambrosini, 2006) and data necessary to estimate damping in field settings are extremely scarce. For high-quality (i.e. massive) slender landforms such as rock arches and towers, damping has been shown to be low (∼1-3% of critical; Moore et al., 2019; Geimer et al., 2020) but can reach values of 8-10% for fractured rock slopes (Häusler et al., 2021) and, thus similar to engineered structures with significant soil-structure interaction such as arch dams (Chopra, 2012b). Since eigenmode displacements of mountains under ambient excitation are generally small (nanometers to micrometers), and because energy dissipation by joint deformation is also expected to be small for high confining pressures at depth, we predict that material damping is comparably minor and radiation damping dominates as influenced by geometry (for further discussion see Häusler et al., 2021). While slender towers with large vertical-to-horizontal aspect ratios have low damping, mountain landforms with lower aspect ratios are likely to experience greater radiative energy loss. Damping ratios are, in turn, inversely related to amplification (Chopra, 2012a), therefore the anticipated higher damping for Alpine mountains may reduce topographic amplification. On the other hand, higher damping broadens the spectral peaks of resonant modes, potentially widening the frequency band susceptible to topographic amplification.

Here we present new ambient seismic data from two mountains in the Swiss Alps (the Matterhorn and Grosser Mythen), similar in shape but vastly different in scale, each of which exhibits large spectral amplification (values of ∼10 and greater) that we attribute in part to excitation of fundamental and higher order resonant modes in a topographic resonance effect. Our data further show these mountains exhibit high modal damping ratios resulting from efficient energy radiation, which reduces spectral amplification but widens the amplified frequency band. Ambient vibration modal analysis and eigenfrequency modeling confirm the measured frequency-dependent polarization attributes. At the Matterhorn, we analyzed 13 months of continuous data, showing that spectral peaks are stable over time and that the fundamental frequency of the mountain does not measurably vary. Our results aid estimation of topographic amplification for other mountain features by providing likely upper limit values (for large-scale landforms), as well as new information on damping, while demonstrating that eigenfrequency modeling can be used to approximate the resonant frequencies of mountains. When excited, high-relief mountains may experience large amplification of ground motion, making these areas more prone to earthquake-triggered rock mass damage and slope failure (Gischig et al., 2015).

2. Study sites

We deployed three broadband seismometers on the eastern flank of the Matterhorn, Canton Valais, Switzerland, in summer 2019 (Fig. 1). We used 3-component Nanometrics Trillium Compact 20 s seismometers with Centaur data loggers, each powered by a local solar power system, recording continuous data at 250 Hz. Sensors were leveled and aligned to north, and data streamed in real-time via local Wireless LAN to the Internet (Weber et al., 2019). We deployed one seismometer at 4470 m asl just below the summit of the Matterhorn (station code MH54), one seismometer at 4003 m asl on the Hörnli ridge at the Solvay hut (station MH48), and one reference station on flat bedrock at 2944 m asl in the glacier forefield at the foot of the mountain (station MH52; Fig. 1 and Table S1). The horizontal distance between the summit and reference station was 3.2 km, and the elevation difference was 1526 m. Care was taken in all cases to prepare a safe and stable station foundation by removing loose rock and identifying solid bedrock as much as possible. All sensors were encased in a small vault built on site (Figure S1). At the Solvay hut, we cut through the floor of the hut, removed underlying rock and ice, and then laid a thin layer of concrete to create a flat seismometer foundation. All sensors operated semi-continuously, with only minor data outages caused by lack of power due to prolonged poor weather (Table S1 and Figure S2 describe data availability for each sensor). The date range of operational overlap for all three sensors was August 27 – October 15, 2019, limited primarily due to deep snow cover at the reference station.

In addition to our primary experiment at the Matterhorn, we deployed a temporary array of three 3-component seismometers on the Grosser Mythen, Canton Schwyz, Switzerland (Figure S3). The Grosser Mythen shares a similar horn-like shape as the Matterhorn, but is far smaller, serving as a down-scaled topographic analog with easy access. We placed two Nanometrics Trillium Compact 120 s seismometers at 1875 and 1887 m asl on the summit of the Grosser Mythen (station codes MYT003 and MYT004), and one Lennartz LE-3D 5 s seismometer at 1444 m asl at the base as a reference station (MYT001). The horizontal distance and elevation difference between the highest summit station and the reference was 450 m. For each station, we first dug a small pit to remove loose topsoil and rocks, then leveled and aligned the sensors using a tripod firmly pressed into the underlying soil. The sensors collected 2 hours of concurrent data on July 24, 2019, logged locally on Nanometrics Taurus dataloggers. Full sensor and deployment metadata are given in Table S2.

3. Methods

Frequency-dependent polarization analysis of each mountain array used waveforms from all stations converted to acceleration by deconvolving the instrument response provided by the IRIS DMC Library of Nominal Responses for Seismic Instruments. The Fourier amplitude spectrum and power spectral density were estimated for non-overlapping hour-long windows (3600 s) of each component on all three seismometers. Stable spectral estimates were obtained with Welch's method, averaging over 655.36 s segments overlapping by 75%, with a 10% cosine taper applied to each end. The spectral amplitude ratio between the common components of two stations represents the relative, frequency-dependent amplification of a station with respect to another station (Spudich

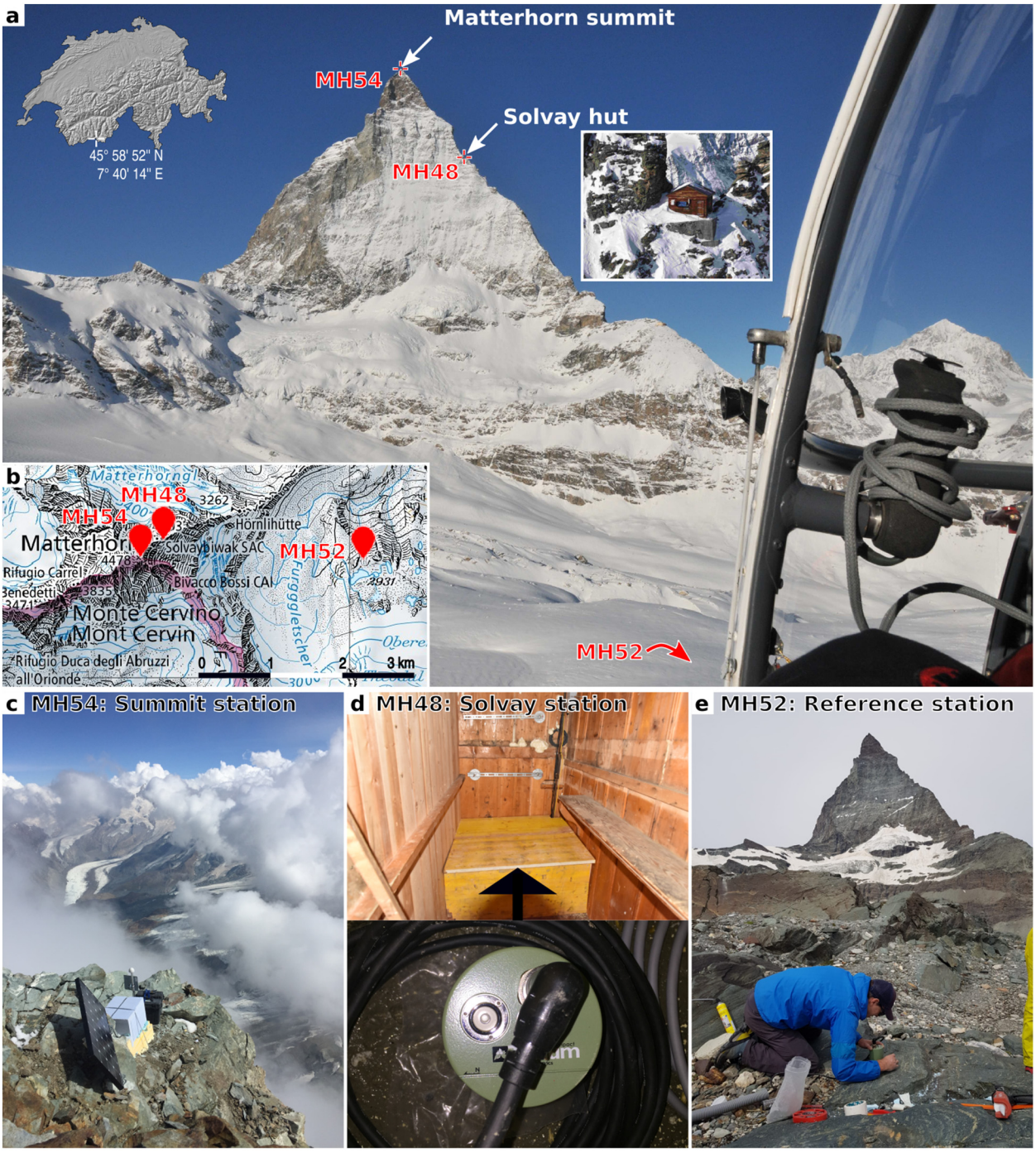

Fig. 1. Overview of the Matterhorn study site and sensor installations. a) Oblique aerial image showing the east flank of the Matterhorn with the Hörnli ridge on the horizon right of the summit. Seismic stations were installed on the summit (MH54) and Solvay hut (MH48), with a local reference station located in the proximal glacier forefield (MH52). Study area location within Switzerland shown in inset. b) Topography of the study area (geodata source: Federal Office of Topography) with station locations indicated. c-e) Photographs of seismic stations.

et al., 1996). Polarization attributes were computed using the "Frequency dependent polarization analysis bundle" (IRIS DMC, 2015). The probability density functions of the three primary polarization attributes (β^2, Θ_H and Θ_V) were estimated following Koper and Hawley (2010). β^2 describes the degree of polarization and measures the extent of spatial organization in the recorded waveforms. Θ_H and Θ_V describe the orientation of the polarization ellipsoid. Finally, histograms were calculated using all hour-long windows, with a period bin step of 1/50 octave and a period smoothing width of 1/10 octave, enabling calculation of probabilistic power spectral densities, site-to-reference amplitude spectral ratios, and polarization attributes.

Frequency-dependent, empirical absolute amplification for each mountain station was determined through automated analysis of earthquake recordings following the empirical spectral modeling (ESM) method of Edwards et al. (2013). The technique compares the spectra observed by the Swiss national seismic network with the expected spectra of a source and path model valid for the Swiss reference rock condition (Poggi et al., 2011). The model is used to retrieve damping and local site amplification relative to the

regional reference rock model, defined by the 27 seismic stations where the shear wave velocity profile is known. The elastic site amplification is computed by the geometric mean of all observations on the horizontal components when the signal-to-noise ratio exceeds three. Due to lower signal-to-noise ratios at lower frequencies, fewer observations contribute to the amplification curve. No results exist for frequencies less than 0.5 Hz due to the lack of a predictive model (Edwards et al., 2013). In our study, up to 57 and 25 seismic events contributed to the ESM amplification function of stations MH48 and MH54, respectively. Due to the short installation period of the reference station (MH52), only two observations were available, providing insufficient data to compute reliable amplification values.

We quantified modal attributes using Frequency Domain Decomposition (FDD) analysis, an output-only technique used to determine the frequencies and shapes of a system's normal modes. The approach was introduced by Brincker et al. (2001a) to experimentally evaluate the dynamic response of engineered structures (e.g. Michel et al., 2008). In the past decade, the technique has found additional application on natural features, such as sedimentary valleys (Ermert et al., 2014; Poggi et al., 2014), rock towers (Moore et al., 2019), and slope instabilities (Bottelin et al., 2013; Häusler et al., 2019). The method applies a singular value decomposition of the complex cross-power-spectral density matrix of all three-component recordings simultaneously measured on a structure. Plotting the singular values (SV) allows for determination of resonant frequencies, with the first SV indicating the dominant mode and higher SV indicating secondary modes. Evaluating the singular vector at a resonant frequency provides direct measurement of modal deflection. An advantage of FDD is that only one plot needs to be analyzed for an array, containing information from all recordings and preserving phase information, simplifying detection of higher modes. Furthermore, the analysis of higher SV and singular vectors allows for detecting close and hidden modes that are difficult to resolve with conventional spectral analyses. The Enhanced Frequency Domain Decomposition (EFDD) technique (Brincker et al., 2001b) additionally estimates modal damping ratios by transforming the mode bell attributed to a natural frequency (using the Modal Assurance Criterion, Allemang, 2003) to the time domain and obtaining the impulse response function. The damping ratio is then computed by the logarithmic decrement technique (Chopra, 2012a). FDD requires ambient vibration data with near-constant spectral density across the band of natural frequencies of interest. Violation of this assumption leads to forcing of specific frequencies that do not represent natural modes of the structure.

We modeled the 3D modal behavior of each mountain using COMSOL Multiphysics (comsol.com) to predict eigenfrequencies and modal displacement fields. We first extracted relevant digital elevation data from the Swiss national 25m-resolution DEM (geodata source: Federal Office of Topography), which we transformed into smoothed and cropped 3D solids. We assumed a uniform density of 2.7 g/cm^3 for gneiss of the Matterhorn and limestone of the Grosser Mythen (Goodman, 1989), and performed a series of 3D eigenfrequency simulations (note these frequency-domain models do not simulate wave propagation and do not use or require material damping). Two approaches were used to approximate the Young's modulus of the mountain-scale rock masses: uniform and pressure-dependent. The uniform approach, based on Geimer et al. (2020), used forward modeling to determine the homogenous modulus that best reproduced the resonant frequencies and polarization attributes from field data. We implemented fixed lateral and bottom boundaries in these models (which were performed without gravitational stresses), ensuring boundaries were sufficiently far from the mountains to avoid influencing the eigenmodes. We additionally used ultrasonic velocity measurements on rock samples from the Matterhorn to check the validity of our assumed uniform modulus (Aydin, 2014). The pressure-dependent approach, newly employed in this study, was developed based on P-wave velocity depth profiles from Brocher (2008). We implemented a Young's modulus that increased with pressure according to a sigmoid function controlled by three parameters: minimum modulus (at the surface), transition zone width (in units of pressure), and maximum modulus (at the bottom of the transition zone). The approach was applied in COMSOL using an iterative workflow for model stability. Beginning with a homogenous model using the minimum modulus and lateral roller boundaries to allow settlement, we solved the static stress field under gravitational loading. We then used this solution to calculate the pressure-sensitive modulus field, increasing the modulus contrast by 20% per iteration and using each subsequent solution to calculate the modulus distribution for the next iteration. The final full-contrast model was reached in the fifth iteration, which we used as input for eigenfrequency analysis. For both approaches, we extracted the eigenvectors at the positions of our seismometers to compare against observed values.

4. Results

Power spectral densities are displayed in Fig. 2 for the period of operational overlap (August 27 – October 15, 2019) of all Matterhorn stations and channels. Probabilistic analysis of hour-long intervals shows the dominant spectral content of each record is consistent over time. Figures S4–S7 show spectra from the summit and Solvay stations over 10 and 13 months of monitoring, respectively, demonstrating stability despite seasonal changes in near-surface environmental conditions. All stations and channels exhibit energy around 0.2 Hz associated with the secondary microseism, created by deep-water interactions of propagating ocean waves (Koper and Hawley, 2010) (Figure S8). Below this frequency range, variations in spectral power occur as a function of teleseismic activity. Above ~0.3 Hz, records from the two mountain stations begin to diverge from the reference. Station MH52 – the reference – remains at low power, paralleling the low noise model (Peterson, 1993) with no distinct spectral content until well above 1 Hz, indicating the station is a high-quality reference. On the other hand, stations MH48 at the Solvay hut and MH54 on the Matterhorn summit, show evidence of increased spectral power across a relatively broad band from 0.4 to 1 Hz (and greater), especially notable on the horizontal components. However, because this energy occurs on the 'shoulder' of the microseism, it is partly obscured. Varying anthropogenic signals are also visible at times in the spectra.

To explore evidence of eigenmodes in our data, we performed FDD analysis using 24 h of representative data from September 20, 2019. The results (Fig. 3a-c) show clear indication of a resonant mode of the Matterhorn at 0.42 Hz, as well as a second, non-dominant mode in this same frequency range. The second mode is evident from the second singular value curve (see interpreted mode bell in Fig. 3), which is elevated above the noise level (i.e. third and higher singular values). The first (dominant) mode exhibits sub-horizontal ground motion at an azimuth of 155° (summit modal vector azimuth / incidence: 155° / 88°), while the second mode displays near perpendicular sub-horizontal motion (summit: 72° / 87°). However, estimation of the mode shape of the second mode is biased due to the orthogonality principle of the singular value decomposition and the proximity and high damping of the two modes. Modal vectors for the summit and Solvay stations were similar for each mode, with azimuthal differences of <4°. EFDD analysis further reveals both resonant modes exhibit high damping ratios of around 20%. We confirmed FDD results and explored the stability of our measurements over the full

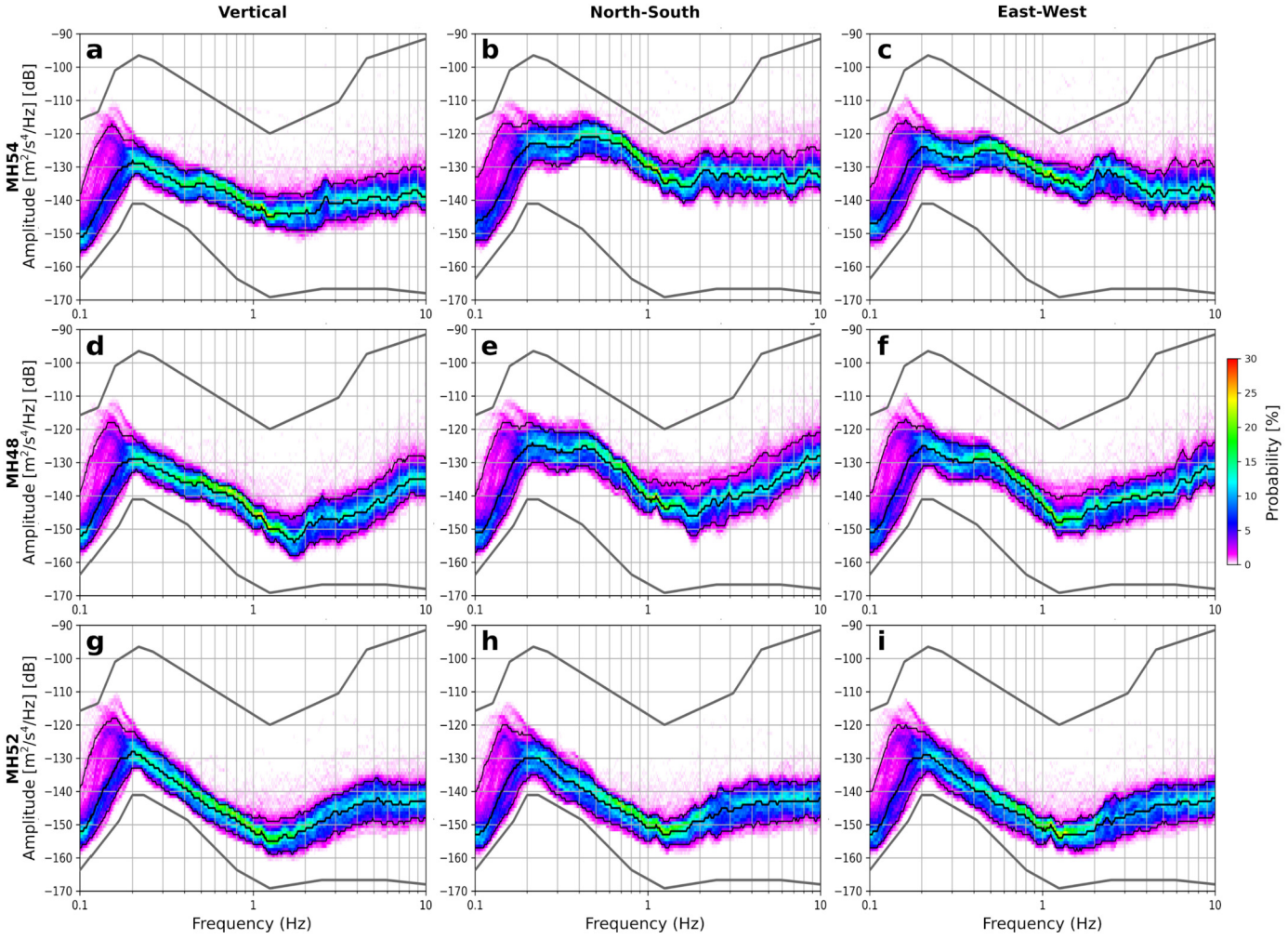

Fig. 2. Probabilistic power spectral density plots of all stations and station components during the period of operational overlap: 27/08 – 15/10, 2019. a-c) Summit station MH54, d-f) Solvay station MH48, g-i) Reference station MH52. Ambient vibration data were processed in hour-long intervals. High and low noise models (Peterson, 1993) included for reference. Probability indicated by color scale, 5/50/95-percentile for each shown in black solid lines. (For interpretation of the colors in the figure, the reader is referred to the web version of this article.)

frequency range using frequency-dependent polarization analysis (Fig. 3d-i). The Matterhorn summit station exhibits a clear peak in polarization between ~0.4-0.8 Hz (β^2 values up to 0.6), with sub-horizontal ground motion (incidence of 80°-85°) and a dominant azimuth of ~155°, while the reference station exhibits low polarization (values <0.2) with no preferred orientation of ground motion in this band. Apparent 180° differences in the dominant azimuths recorded at the summit and Solvay stations arise from vector polarization ambiguity during horizontal motion (incidence >80°; Geimer et al., 2020). Probabilistic analyses show these values were consistent over the measurement period (Figure S9).

To further analyze spectral content and quantify directional spectral amplification, we calculated site-to-reference spectral amplitude ratios comparing each of the two mountain stations to our reference (Fig. 4). Because the reference station had relatively flat and quiet spectra, spectral ratios were unaffected by artifacts (e.g. peaks or holes) created by spectral division. We present rotated spectral ratios in Fig. 4, where we selected the dominant polarization azimuth (155°) to display values. Results reveal strong amplification between 0.4-2 Hz, with median spectral ratios on the Matterhorn summit reaching peak values of 14 at 0.7 Hz. The ratios further show that this frequency band experiences broad amplification with few distinct peaks. At the identified fundamental frequency of 0.42 Hz, rotated site-to-reference spectral ratios indicate an amplification factor of 9 at the Matterhorn summit and 5 at the Solvay station. Minor differences between the 5th and 95th percentile curves in this frequency range support consistency of these spectral ratios over time, and indicate that time-varying environmental effects (such as wind, see Figure S8) do not strongly influence these values at the large-scale mountain site (see also Figure S4). Separately calculated horizontal to vertical amplitude spectral ratios (Figure S10) support these observations and show similar results, as do results from spectral amplification measurements from earthquake records (Figure S11), even though the frequency band in that analysis could not be extended below 0.5 Hz. We note, however, that amplification functions shown in Figure S11 are not directly comparable to site-to-reference spectral ratios calculated from our data because they refer to the Swiss reference rock velocity profile (mostly sedimentary rocks), while our local reference site is likely characterized by higher shear wave velocities (crystalline rocks).

We used numerical eigenfrequency analysis to further explore the first resonant modes of the Matterhorn. We compared the results of two models: 1. a simple model assuming uniform Young's modulus of 35 GPa, and 2. a model implementing a pressure-dependent Young's modulus varying from 7-35 GPa over a pressure range of 0-20 MPa. Results from the two models were similar: in each case, mode 1 occurred at 0.43 Hz and consisted

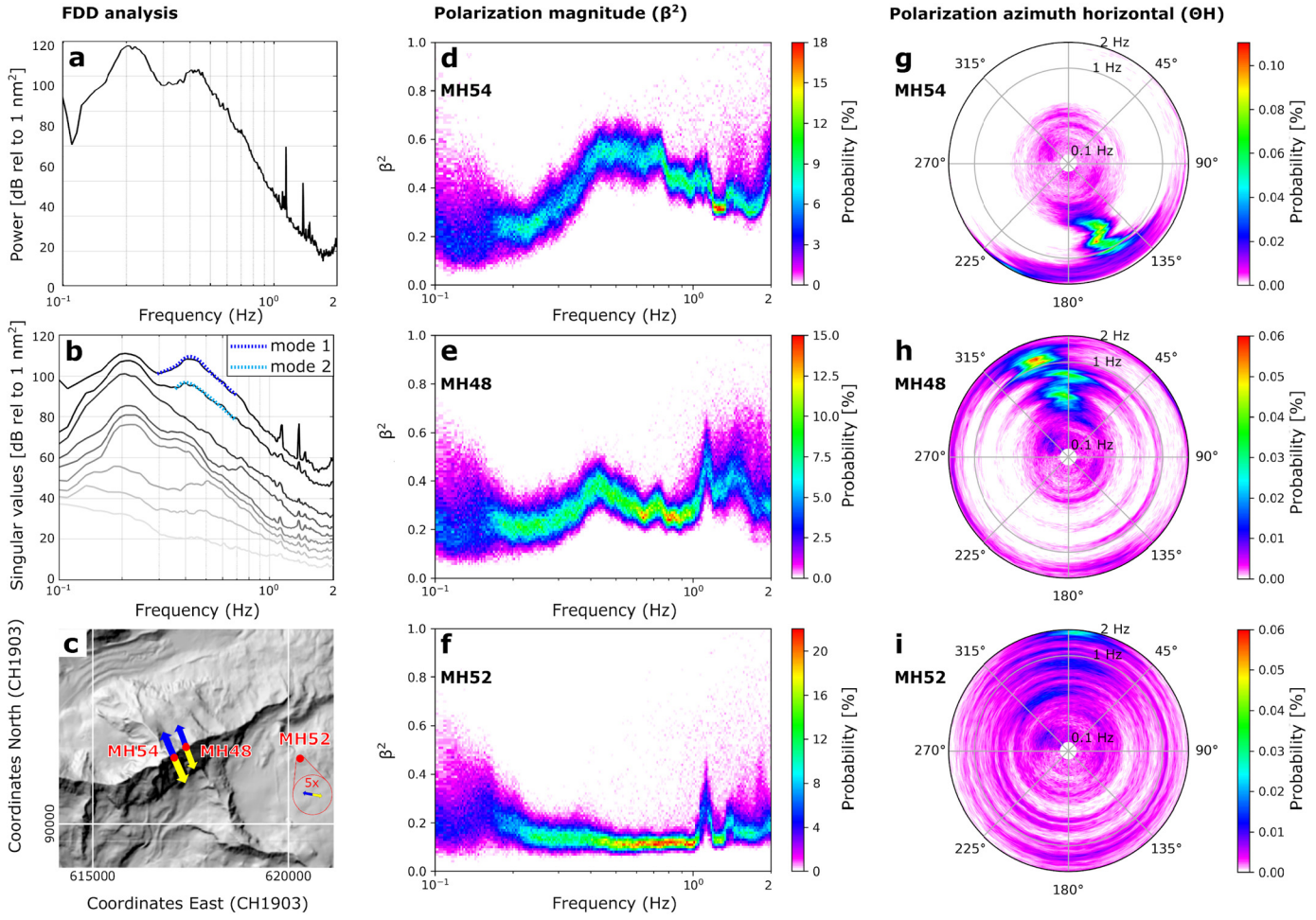

Fig. 3. FDD modal analysis and polarization results. a) Power spectrum as well as b) singular value plot with interpreted mode bells (colored lines for mode 1 and 2) and c) a map (geodata source: Federal Office of Topography) illustrating the FDD vectors (shapes for the first mode) for Matterhorn array data from September 20, 2019, Polarization results for all data shown in probabilistic visualizations for all stations: d-f) degree of polarization and g-i) polarization azimuth (incidence angles are predominantly horizontal and thus not shown; see Figure S9). (For interpretation of the colors in the figure, the reader is referred to the web version of this article.)

of approximately north-south horizontal motion of the mountain, while mode 2 occurred at 0.46 Hz showing perpendicular, approximately east-west motion (Figure S12). The pressure-dependent model showed a slight rotation of modal vectors (4° clockwise) and a 6% smaller summit-to-Solvay amplitude ratio. Because results from the two modeling approaches were so similar, we opt to describe outputs from the simpler, uniform model (Fig. 5 and supplemental animations). Modeled modal vectors are in good agreement with FDD results for points extracted from the model at the summit (azimuth / incidence: mode 1 = 166° / 89°; mode 2 = 87° / 85°) and Solvay hut stations. Moreover, the modeled ratio of modal amplitudes for the summit to Solvay positions was 1.7 for the fundamental mode, similar to the ratio of measured amplification (1.8). Model results additionally predicted a number of higher order modes between 0.5-0.7 Hz, including a vertical (or axial) elongation mode, but these were not clearly evident in our field data, possibly due to limited spatial sampling, and thus cannot be validated. Extending the model boundaries far from the mountain in the uniform case had no effect on the first eigenmodes (as in Moore et al., 2018), while the more complex pressure-dependent model required slightly smaller lateral extents in order to converge (see Figure S12).

As a smaller topographic analog to the Matterhorn, we analyzed ambient vibration data from the Grosser Mythen using the same approaches. Power spectra and FDD analysis revealed two resonant frequencies of the mountain at 1.8 Hz and 2.3 Hz, which we characterized using EFDD (Fig. 6a, b). Modal vectors showed predominantly horizontal deflection of the mountain in different directions (azimuth / incidence = 103° / 83° and 133° / 82° for modes 1 and 2, respectively), and modal damping ratios were again high, ~16% for mode 1 and ~20% for mode 2. The summit station reached a peak site-to-reference spectral amplification factor of 6 in the dominant polarization direction. We additionally performed eigenfrequency modeling for the Grosser Mythen, and obtained a good match with the measured fundamental frequency implementing a uniform Young's modulus of 70 GPa (Fig. 6d). We were unable to satisfactorily match the second observed mode in our model.

5. Discussion

We investigated spectral amplification of ambient ground motion at two large-scale mountain landforms. At the Matterhorn summit, we observed strong directional amplification in a band between 0.4-1 Hz, with spectral ratios >10 at an azimuth of 155°. Spectral ratios were slightly lower at the Solvay hut (Fig. 4). Spectral ratio processing adequately removed the influence of the microseism, which obscured standard power spectra visualizations of modal frequencies (Fig. 2). Probabilistic processing further demonstrated stability of spectral attributes over time, during both the ~6-week period of array overlap and the 10 and 13 months of continuous data from the summit and Solvay stations, respectively (Figures S7 and S8). At the Grosser Mythen, we observed

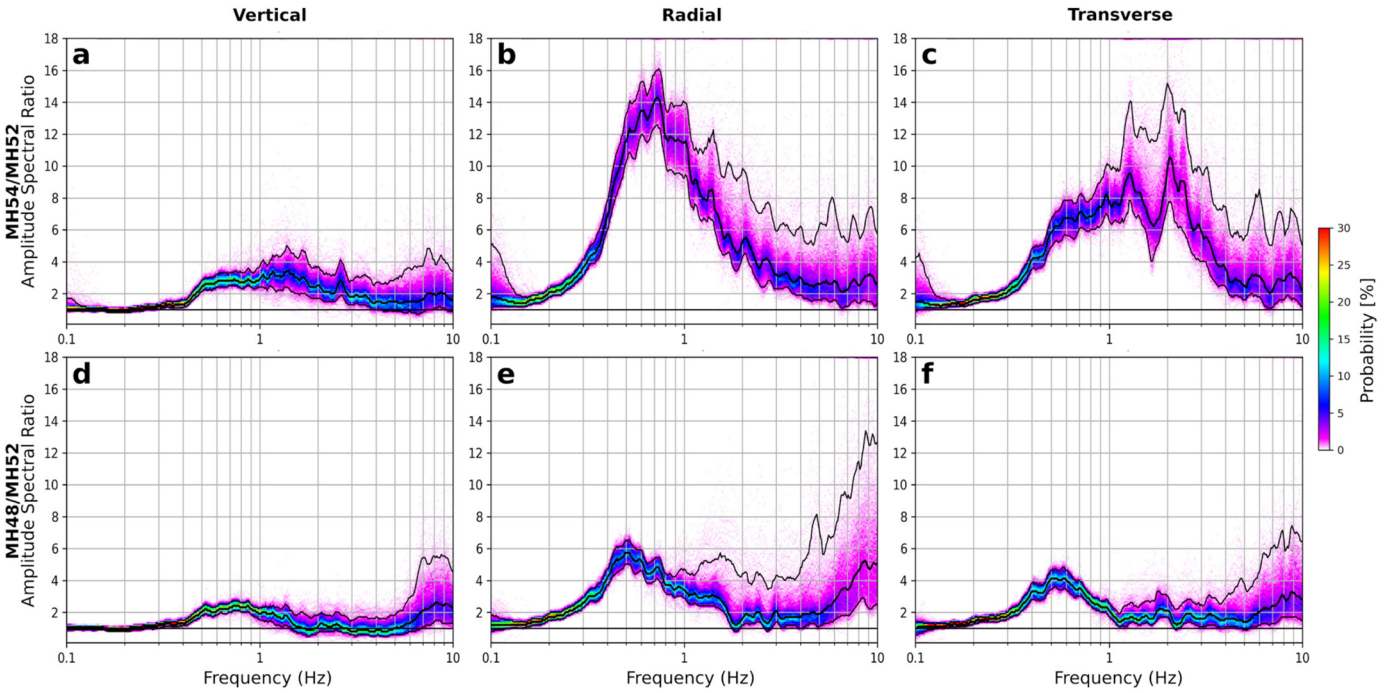

Fig. 4. Probabilistic amplitude spectral ratios, rotated to the dominant modal azimuth of 155°, for the a-c) Summit (MH54) and d-f) Solvay (MH48) stations as compared to the reference (MH52). Probability indicated by color scale, 5/50/95-percentile for each shown in black solid lines. (For interpretation of the colors in the figure, the reader is referred to the web version of this article.)

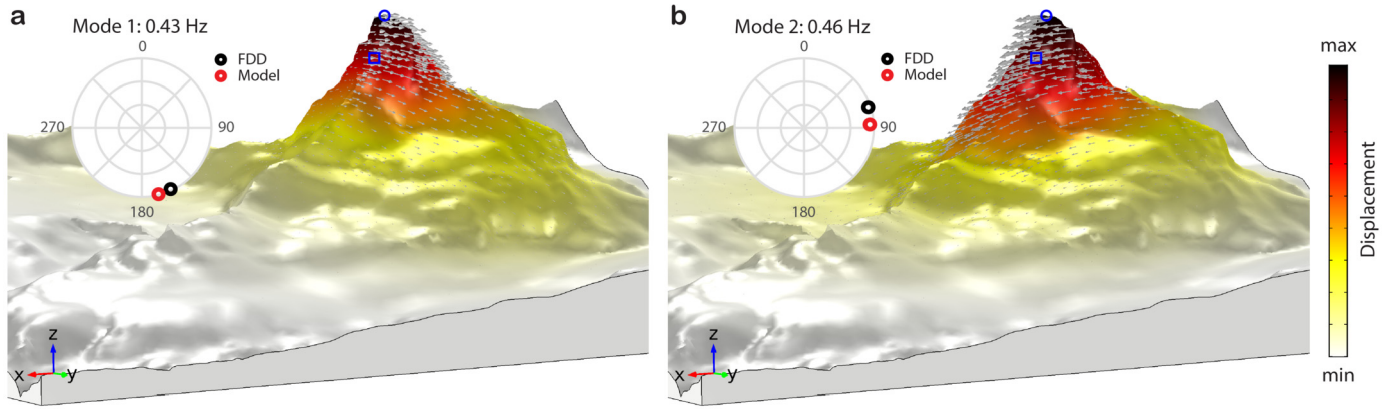

Fig. 5. Numerical eigenfrequency analysis of the Matterhorn assuming a uniform elastic modulus (cf. Figure S12): a) Mode 1, b) Mode 2. Relative modal displacements shown by color scale and arrows, modeled eigenfrequencies are indicated. Inset polar plots show comparison of modal vectors for the summit station (MH54) for FDD and numerical results (circumferential axis: azimuth; radial axis: incidence from 0° at center to 90° - horizontal - at outer). Summit (circle) and Solvay (square) stations are indicated. (For interpretation of the colors in the figure, the reader is referred to the web version of this article.)

a higher fundamental frequency of 1.8 Hz, consistent with the smaller size of the mountain, with spectral ratios up to 6 on the summit (Fig. 6). We note that if the geometry of the Matterhorn was downscaled such that its mass (∼9E12 kg) was equal to that of the Mythen (∼5E11 kg) with the same material properties, the anticipated fundamental frequency would be 1.7 Hz. This close agreement is, however, partly coincidental as the form of the two mountains is not identical and our eigenfrequency modeling suggests the Mythen has greater Young's modulus consistent with the limestone lithology. While the Young's modulus estimated for the Mythen is comparably high at 70 GPa, we note that limestone is frequently stiffer than metamorphic rocks, and 70 GPa is within the upper range of past reported laboratory values (e.g. Goodman, 1989; Bell, 2007).

We observe that peak site-to-reference spectral ratios at the Matterhorn do not occur at the identified fundamental frequency, rather at slightly higher frequencies in the amplified band (compare Figs. 3 and 4). This observation may be explained by one or a combination of factors: 1) the reference station experiences modal deformation at the fundamental mode (with the greatest wavelength) but not at higher-frequency modes with shorter wavelengths, meaning the spectral ratio measurements underestimate 'true' fundamental-mode amplification; 2) Modal deformation is stronger at the summit station for higher-order resonant modes, perhaps caused by geometric filtering favoring shorter wavelengths (wave focusing); 3) The reference station spectra is adversely affected by some noise source, causing either apparent deamplification of lower frequencies or amplification at higher frequencies (unlikely). We suspect the first option is possible, and that had this station been located farther from the mountain, amplification in the 0.4-0.5 Hz band could have been greater (assuming similar site conditions). We further anticipate that complex 3D wave propagation effects, possible dependencies on the azimuth of incident waves, and wave focusing factor in at higher frequencies (e.g.

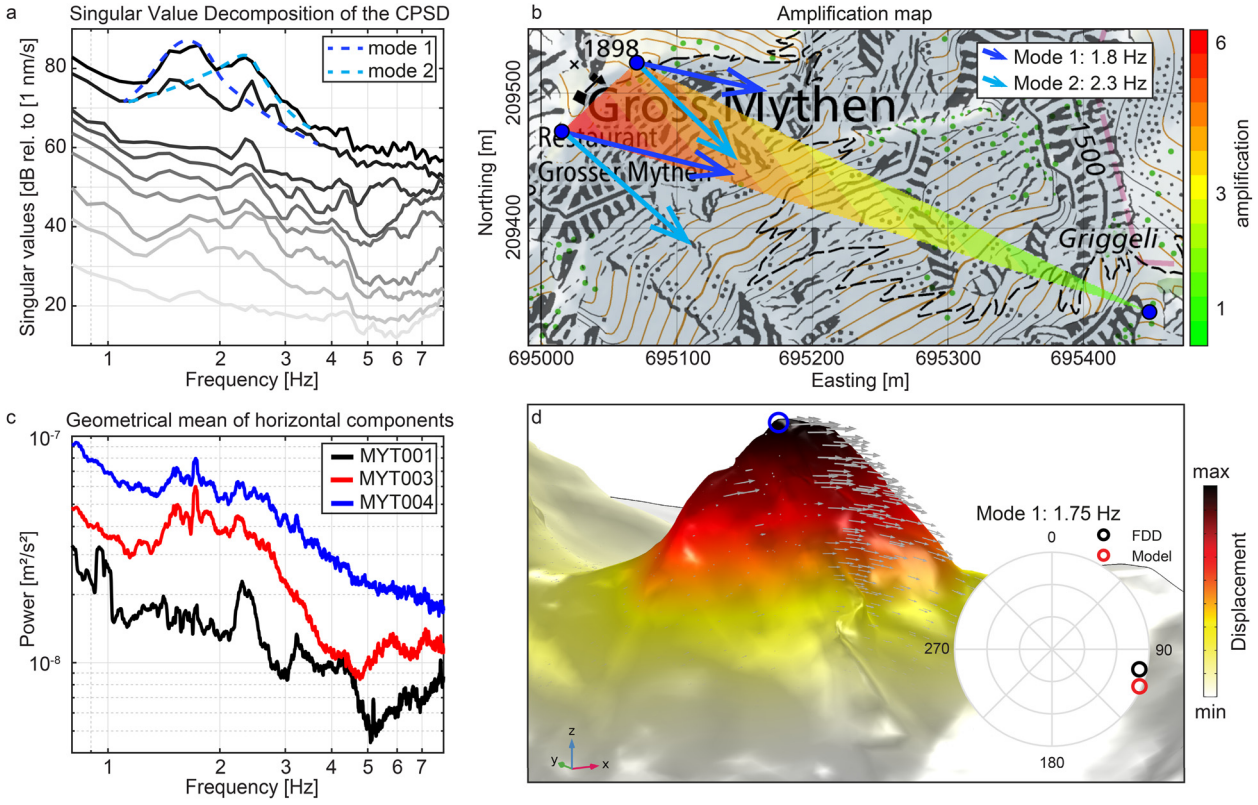

Fig. 6. a) Singular value plot resulting from FDD modal analysis of ambient vibration measurement at Grosser Mythen. b) Normal mode shapes for the first and second mode (arrows) and amplification map based on site-to-reference spectral ratio (geodata source: Federal Office of Topography). c) Power spectra of all temporary stations, geometrical mean of both horizontal components. d) Numerical eigenfrequency analysis of Mythen, showing the normal mode shape of the fundamental mode at 1.75 Hz. Inset polar plot shows the comparison of modal vectors for the summit station (MYT004) for FDD and numerical results (circumferential axis: azimuth; radial axis: incidence from 0° at center to 90° - horizontal - at outer). Summit station (MYT004) position indicated (blue circle). (For interpretation of the colors in the figure, the reader is referred to the web version of this article.)

Lee et al., 2009), helping elevate the spectral amplification values in the band between ∼0.5-1 Hz.

Site-to-reference spectral ratios in the range of 10 have been observed at other topographic sites, however rarely for such large-scale mountain landforms. For example, large spectral ratios of ∼6 were measured at the fundamental resonant frequency of a ∼50 m high mesa in New Mexico (Stolte et al., 2017), and in the extreme limit of a slender 120 m high rock tower, values of ∼70 were predicted (Moore et al., 2019). However, for large-scale topographic forms, spectral amplification is generally much lower. LeBrun et al. (1999) reported amplification factors of 2-3 at the fundamental frequency (∼0.7 Hz) of a 700 m high hill in Greece. Other similar studies are summarized by Massa et al. (2014), showing a common maximum range of spectral amplification between 3-5 for landforms with resonant frequencies of ∼1-3 Hz. Comparison indicates our measurements represent relatively large measured topographic effects, at one of the largest landforms assessed, and similarly place lower bounds on the observed resonant frequencies of mountains. Large spectral ratios reported from other topographic array studies, however, must often be treated with caution. First, suitable selection of a reference station is not always feasible, and spectral ratios can be contaminated by processing or noise artifacts. Second, distinguishing coupled site effects created by subsurface velocity contrasts in such measurements has also proven challenging (Burjánek et al., 2014; Rault et al., 2020). While the two mountains studied here each feature a lithologic contact at high elevations (geodata source: Federal Office of Topography), shear wave velocity contrasts across these rock-type transitions are likely to be comparably small and unlikely to generate the large spectral amplifications measured.

We propose that the spectral amplification evident in our ambient vibration data results to the first order from resonance of the large-scale mountain landforms. We used FDD analysis to determine properties of the eigenmodes in our data. For the Matterhorn, we were able to distinguish the fundamental mode at about 0.42 Hz exhibiting subhorizontal modal displacements oriented at an azimuth of 155°, and another closely spaced mode consisting of mutually perpendicular horizontal motion (Fig. 3). We note that the 155° orientation is roughly perpendicular to the crest of the Matterhorn massif connecting the Cresta del Leone and Hörnli Ridge, suggesting the fundamental mode is deforming against the mountain's slightly more slender ∼N-S width. The FDD approach has been previously used to study resonance of rock slope instabilities, civil structures, and sedimentary basins (Michel et al., 2010; Poggi et al., 2014; Häusler et al., 2019). One benefit is the ability to distinguish closely spaced modes, which was critical at our mountain study sites with near radial-symmetric form. Without such processing, discerning modal properties of the Matterhorn from interpretation of conventional spectral plots alone may not have been possible. While we characterized the first two resonant modes of the mountain, we believe other eigenfrequencies are represented in our measurements. Our numerical models predicted several additional modes between 0.5-1 Hz, however, we were unable to distinguish these in our data, possibly due to sparse spatial sampling. Other possible sources of spectral amplification, such as localized compliant rock fractures related to localized slope instabilities (e.g. Moore et al., 2011), were not observed at our study sites and are thus unlikely to influence our results.

One benefit of our modal analysis is the ability to calculate damping. For both mountains, we determined modal damping ra-

tios of ∼20%, far higher than previously observed at smaller-scale geological landforms (e.g. Moore et al., 2019; Geimer et al., 2020; Häusler et al., 2021). Since our data are unaffected by large-scale slope instabilities and because these mountains exhibit only minor lithological contrasts, we interpret the large difference in damping between slender rock towers (∼1%) and the Matterhorn and Mythen (20%) to arise primarily from differences in geometry. Both mountains show a large cross-sectional basal area compared to their height, facilitating energy radiation out of the feature. Damping plays a key role in controlling spectral amplification and the width of resonant frequency bands, however it is rarely (if ever) determined from field measurements of topographic and site effects. While damping and spectral amplification are theoretically linked (Moore et al., 2019), damping estimation using EFDD does not require a (potentially biased) reference station as in calculation of spectral ratios. Thus, damping resolved from EFDD might be useful as an independent approach to estimate amplification. Damping is in turn a necessary input for dynamic numerical modeling, which is rarely parameterized by measurements, and additionally affects the duration of strong ground motion during earthquakes. We propose that high modal damping measured for mountain landforms results primarily from radiative effects, i.e. loss of energy due to the open-based form of topography, rather than material damping.

The two numerical models used to explore resonance properties of the Matterhorn resulted in similar outcomes, suggesting that the added complexity of our more detailed pressure-dependent model was not required to match basic modal properties (Figure S12). While the approach likely better represents the mechanical conditions of in-situ bedrock – allowing Young's modulus to increase with pressure – the added complexity resulted in longer model run times and more challenging set up. Implementing pressure-dependent Young's modulus reduced stiffness in the near-surface, but ultimately had little impact on the first eigenmodes as the majority of the volume was at higher pressures. This outcome suggests that for models of large-scale landforms, stiffness of the deeper core of the mountain plays the dominant role in controlling the eigenfrequencies, while stiffness of the outer shell is less important. Differences to a uniform model might be more pronounced at higher modes, e.g. modes involving just the summit of the Matterhorn. The further implication is that even basic eigenfrequency modeling assuming uniform material properties can be adequate for estimating the modal properties of mountains (Fig. 5). In our case, we could confirm the assumed Young's modulus with laboratory ultrasonic velocity testing on rock samples taken at the Solvay hut and Hörnli ridge at 3500 m asl (Weber et al., 2019), which showed an average (unfrozen, dynamic) Young's modulus of ∼20 GPa, reasonably close to our implemented value of 35 GPa. We note, however, that high-frequency ultrasound testing may generate Young's modulus estimates that are not absolutely comparable to our model back-analysis approach based on low-frequency resonance data.

Resonant frequency drifts have been previously reported for shallow or slender rock landforms experiencing changing temperature and ice content conditions (e.g. Bottelin et al., 2013; Weber et al., 2018; Häusler et al., 2021), and could be expected for the Matterhorn if the outer rock shell experiencing seasonal changes controls the dynamic properties of the mountain. Ice in particular has been shown to stiffen rock masses leading to a marked increase in resonant frequencies, and could play an important role at the Matterhorn which experiences annual changes in the permafrost active layer (e.g. Weber et al., 2019). However, our data reveal no conclusive evidence of seasonal frequency wander, indicating that changes in near-surface (i.e. several meters deep) conditions do not significantly affect the resonance properties of the entire mountain. Rather our results suggest it is more likely the deep bedrock at the core of the mountain, unaffected by seasonal changes in temperature, water and ice content and likely the stiffest structural component, control the first eigenmodes. Higher order modes may be more sensitive to near-surface coupled mechanical effects, but are not clearly resolved from our analyses. This observation similarly supports the assumption of a uniform Young's modulus in numerical modeling, as opposed to assuming more complex temperature-dependent material properties.

Results of our study demonstrate that large spectral amplification can be expected when incoming seismic energy is able to excite the resonant modes of mountain landforms, with implications for seismic slope stability. On the one hand this effect is anticipated to be widespread (albeit to varying magnitude), and ample evidence of topographic control on the location of earthquake triggered landslides (e.g. Meunier et al., 2008) as well as infrastructure damage (e.g. Hough et al., 2010) supports this conclusion. However, we point out that our data only cover small deformations in the linear-elastic regime, and that nonlinear effects during strong ground motion may reduce the magnitude of spectral amplification. Strong-motion data not available in this study would be required to quantify amplifications, and changes thereof, in the nonlinear regime. Our results further provide several key outcomes useful for predicting aspects of topographic amplification of ground motion on mountain slopes and summits, relevant for assessment of earthquake induced landslides: a) likely lower-limit range for resonant frequencies and a possible upper-limit value for spectral amplification related to topographic resonance, b) experimental data showing high modal damping related to efficient energy radiation, and c) confirmation of the utility of simple numerical models to estimate the resonant frequencies of mountain landforms. When excited, tall mountain peaks may shake ∼10 times stronger than adjacent valleys, which likely makes these areas more prone to co-seismic rock damage and landslides. However, more data are needed from additional field studies to quantify how topographic amplification varies with detailed mountain geometry, thus informing predictions relevant for site-specific analysis of earthquake induced landslide susceptibility.

6. Conclusions

We presented new ambient vibration data from two broadband seismic stations installed on the summit and ridge of one the European Alps' tallest mountains – the Matterhorn – which we processed for frequency content and polarization attributes, and compared to a local reference station to identify resonant modes and spectral amplification of ground motion. Our results demonstrate large site-to-reference spectral amplitude ratios across a band between ∼0.4-1 Hz, with peak values up to 14. We used modal analysis and 3D eigenfrequency modeling to explore these data, finding the first two resonant frequencies of the Matterhorn occur at about 0.42 Hz and consist of full-height deflection of the mountain in mutually-perpendicular directions. Our results further indicate high modal damping of ∼20%, which we attribute to radiation energy loss through the base of the mountain. To corroborate these results, we conducted a short measurement on a smaller mountain of comparable form, the Grosser Mythen, finding similar modal attributes and a higher fundamental frequency as anticipated for the smaller scale. Because the Matterhorn represents extreme topography and relief, our results contribute several new instrumental measurements that may help provide limits on estimated topographic amplification of ground motion in other mountain regions, including a possible lower-limit on the fundamental frequency of large-scale mountain forms, possible upper-limit values of spectral amplification caused by topographic resonance, and rare new field estimates of damping. When incoming seismic en-

ergy is able to excite the eigenmodes of topographic landforms, large amplification of ground motion can be expected, with potentially important effects for earthquake-triggered damage and landslides.

CRediT authorship contribution statement

SW, JM, MH and JB in collaboration with all co-authors designed the field experiments. SW, JM, MH, PG, JB and DF prepared the data, performed the analysis and numerical modeling. JM, SW, MH and PG prepared the manuscript with critical revision and final approval from all co-authors.

Declaration of competing interest

The authors declare no conflict of interest.

Acknowledgements

We are grateful to Alessandro Cicoira for assistance during installation of the Matterhorn stations, and to Nora Schweizer for help during field work at the Grosser Mythen. Discussions with Clotaire Michel, Valentin Gischig, Keith Koper, and Michael Krautblatter on concepts of this study are greatly appreciated. We thank IGM Geophysik and Nanometrics for assistance with equipment at the Matterhorn summit station, and Maximilian Lanz and Heiko Käsling for ultrasonic velocity testing tests at the rock mechanics laboratory of the chair for Engineering Geology at the Technical University of Munich. Furthermore we thank the team at Air Zermatt for challenging logistics, Zermatter Bergbahnen for the Internet connectivity and the Swiss Alpine Club SAC as well as the rescue station Zermatt for allowing us to use part of the Solvay hut for the infrastructure supporting this research. Samuel Weber was supported by the Fritz and Lotte Schmidtler-Foundation TUFF fellowship, Mauro Häusler by ETH project 0-20361-17, while Geimer and Moore are supported by NSF project 1831283. Data generated in this study is fully available under https://networks.seismo.ethz.ch/networks/1i/ (University of Innsbruck and WSL/SLF Davos, 2015).

Appendix A. Supplementary material

Supplementary material related to this article can be found online at https://doi.org/10.1016/j.epsl.2021.117295.

References

Allemang, R.J., 2003. The modal assurance criterion–twenty years of use and abuse. Sound Vib. 37 (8), 14–23.
Ambrosini, R.D., 2006. Material damping vs. radiation damping in soil–structure interaction analysis. Comput. Geotech. 33 (2), 86–92.
Ashford, S.A., Sitar, N., Lysmer, J., Deng, N., 1997. Topographic effects on the seismic response of steep slopes. Bull. Seismol. Soc. Am. 87 (3), 701–709.
Aydin, A., 2014. Upgraded ISRM suggested method for determining sound velocity by ultrasonic pulse transmission technique. Rock Mech. Rock Eng. 47, 255–259.
Bell, F.G., 2007. Engineering Geology. Butterworth-Heinemann, Oxford, 581 pp.
Boore, D.M., 1972. A note on the effect of simple topography on seismic SH waves. Bull. Seismol. Soc. Am. 62, 275–284.
Borcherdt, R.D., 1970. Effects of local geology on ground motion near San Francisco Bay. Bull. Seismol. Soc. Am. 60 (1), 29–61.
Bottelin, P., Levy, C., Baillet, L., Jongmans, D., Gueguen, P., 2013. Modal and thermal analysis of Les Arches unstable rock column (Vercors massif, French Alps). Geophys. J. Int. 194 (2), 849–858.
Brincker, R., Zhang, L., Andersen, P., 2001a. Modal identification of output-only systems using frequency domain decomposition. Smart Mater. Struct. 10 (3), 441–445.
Brincker, R., Ventura, C.E., Andersen, P., 2001b. Damping Estimation by Frequency Domain Decomposition. Society for Experimental Mechanics, pp. 698–703 (edited).
Brocher, T.M., 2008. Compression and shear-wave velocity versus depth relations for common rock types in northern California. Bull. Seismol. Soc. Am. 98 (2), 950–968.
Burjánek, J., Moore, J.R., Yugsi Molina, F.-X., Fäh, D., 2012. Instrumental evidence of normal mode rock slope vibration. Geophys. J. Int. 188 (2), 559–569.
Burjánek, J., Edwards, B., Fäh, D., 2014. Empirical evidence of local seismic effects at sites with pronounced topography: a systematic approach. Geophys. J. Int. 197 (1), 608–619.
Çelebi, M., 1987. Topographic and geological amplification determined from strong-motion and aftershock records of the 3 March 1985 Chile earthquake. Bull. Seismol. Soc. Am. 77, 1147–1167.
Çelebi, M., 1996. Radiation damping observed from seismic responses of buildings. In: Proceedings of 12th World Conference on Earthquake Engineering. Auckland, New Zealand.
Chopra, A.K., 2012a. Dynamics of Structures. Pearson Education, Upper Saddle River, NJ, 944 pp.
Chopra, A.K., 2012b. Earthquake analysis of arch dams: factors to be considered. J. Struct. Eng. 138 (2), 205–214.
Davis, L.L., West, R., 1973. Observed effects of topography on ground motion. Bull. Seismol. Soc. Am. 63 (1), 283–298.
Edwards, B., Michel, C., Poggi, V., Fäh, D., 2013. Determination of site amplification from regional seismicity: application to the Swiss National Seismic Networks. Seismol. Res. Lett. 84 (4), 611–621.
Ermert, L., Poggi, V., Burjánek, J., Fäh, D., 2014. Fundamental and higher 2-D resonance modes of an Alpine valley. Geophys. J. Int. 198, 795–811.
Geimer, P.R., Moore, J.R., Finnegan, R., 2020. Sparse ambient resonance measurements reveal dynamic properties of freestanding rock arches. Geophys. Res. Lett. 47, e2020GL087239.
Gischig, V.S., Eberhardt, E., Moore, J.R., Hungr, O., 2015. On the seismic response of deep-seated rock slope instabilities — insights from numerical modeling. Eng. Geol. 193, 1–18.
Goodman, R.E., 1989. Introduction to Rock Mechanics (Vol. 2). Wiley, New York. 562 pp.
Häusler, M., Michel, C., Burjánek, J., Fäh, D., 2019. Fracture network imaging on rock slope instabilities using resonance mode analysis. Geophys. Res. Lett. 46 (12), 6497–6506.
Häusler, M., Michel, C., Burjánek, J., Fäh, D., 2021. Monitoring the Preonzo rock slope instability using resonance mode analysis. J. Geophys. Res., Earth Surf. 126, e2020JF005709.
Harp, E.L., Jibson, R.W., 2002. Anomalous concentrations of seismically triggered rock falls in Pacoima Canyon: are they caused by highly susceptible slopes or local amplification of seismic shaking? Bull. Seismol. Soc. Am. 92 (8), 3180–3189.
Havenith, H.B., Jongmans, D., Faccioli, E., Abdrakhmatov, K., Bard, P.Y., 2002. Site effect analysis around the seismically induced Ananevo rockslide, Kyrgyzstan. Bull. Seismol. Soc. Am. 92 (8), 3190–3209.
Havenith, H.B., Vanini, M., Jongmans, D., Faccioli, E., 2003. Initiation of earthquake-induced slope failure: influence of topographical and other site specific amplification effects. J. Seismol. 7 (3), 397–412.
Hough, S.E., Altidor, J.R., Anglade, D., Given, D., Janvier, M.G., Maharrey, J.Z., Meremonte, M., Mildor, B.S.L., Prepetit, C., Yong, A., 2010. Localized damage caused by topographic amplification during the 2010 M 7.0 Haiti earthquake. Nat. Geosci. 3 (11), 778–782.
IRIS DMC, 2015. Data services products: polarization attributes bundle.
Kleinbrod, U., Burjánek, J., Fäh, D., 2019. Ambient vibration classification of unstable rock slopes: a systematic approach. Eng. Geol. 249, 198–217.
Koper, K.D., Hawley, V.L., 2010. Frequency dependent polarization analysis of ambient seismic noise recorded at a broadband seismometer in the central United States. Earthq. Sci. 23 (5), 439–447.
LeBrun, B., Hatzfeld, D., Bard, P.Y., Bouchon, M., 1999. Experimental study of the ground motion on a large scale topographic hill at Kitherion (Greece). J. Seismol. 3 (1), 1–15.
Lee, S.J., Chan, Y.C., Komatitsch, D., Huang, B.S., Tromp, J., 2009. Effects of realistic surface topography on seismic ground motion in the Yangminshan region of Taiwan based upon the spectral-element method and LiDAR DTM. Bull. Seismol. Soc. Am. 99 (2A), 681–693.
Massa, M., Barani, S., Lovati, S., 2014. Overview of topographic effects based on experimental observations: meaning, causes and possible interpretations. Geophys. J. Int. 197 (3), 1537–1550.
Meunier, P., Hovius, N., Haines, J.A., 2008. Topographic site effects and the location of earthquake induced landslides. Earth Planet. Sci. Lett. 275 (3–4), 221–232.
Michel, C., Guéguen, P., Bard, P.-Y., 2008. Dynamic parameters of structures extracted from ambient vibration measurements: an aid for the seismic vulnerability assessment of existing buildings in moderate seismic hazard regions. Soil Dyn. Earthq. Eng. 28 (8), 593–604.
Michel, C., Guéguen, P., El Arem, S., Mazars, J., Kotronis, P., 2010. Full-scale dynamic response of an RC building under weak seismic motions using earthquake recordings, ambient vibrations and modelling. Earthq. Eng. Struct. Dyn. 39 (4), 419–441.
Moore, J.R., Gischig, V., Burjanek, J., Loew, S., Fäh, D., 2011. Site effects in unstable rock slopes: dynamic behavior of the Randa instability (Switzerland). Bull. Seismol. Soc. Am. 101 (6), 3110–3116.

Moore, J.R., Geimer, P.R., Finnegan, R., Thorne, M.S., 2018. Use of seismic resonance measurements to determine the elastic modulus of freestanding rock masses. Rock Mech. Rock Eng. 51 (12), 3937–3944.
Moore, J.R., Geimer, P.R., Finnegan, R., Michel, C., 2019. Dynamic analysis of a large freestanding rock tower (Castleton Tower, Utah, USA). Bull. Seismol. Soc. Am. 109 (5), 2125–2131.
Panzera, F., Lombardo, G., Rigano, R., 2011. Evidence of topographic effects through the analysis of ambient noise measurements. Seismol. Res. Lett. 82 (3), 413–419.
Paolucci, R., 2002. Amplification of earthquake ground motion by steep topographic irregularities. Earthq. Eng. Struct. Dyn. 31 (10), 1831–1853.
Pedersen, H., Le Brun, B., Hatzfeld, D., Campillo, M., Bard, P.Y., 1994. Ground-motion amplitude across ridges. Bull. Seismol. Soc. Am. 84 (6), 1786–1800.
Peterson, J., 1993. Observations and modeling of seismic background noise. U.S. Geol. Surv. Open-File Rept. 93-322.
Poggi, V., Edwards, B., Fäh, D., 2011. Derivation of a reference shear-wave velocity model from empirical site amplification. Bull. Seismol. Soc. Am. 101, 258–274.
Poggi, V., Ermert, L., Burjanek, J., Michel, C., Fäh, D., 2014. Modal analysis of 2-D sedimentary basin from frequency domain decomposition of ambient vibration array recordings. Geophys. J. Int. 200 (1), 615–626.
Rault, C., Chao, W.A., Gelis, C., Burtin, A., Chang, J.M., Marc, O., Lai, T.S., Wu, Y.M., Hovius, N., Meunier, P., 2020. Seismic response of a mountain ridge prone to landsliding. Bull. Seismol. Soc. Am.
Sepúlveda, S.A., Murphy, W., Jibson, R.W., Petley, D.N., 2005. Seismically induced rock slope failures resulting from topographic amplification of strong ground motions: the case of Pacoima Canyon, California. Eng. Geol. 80 (3–4), 336–348.
Spudich, P., Hellweg, M., Lee, H.K., 1996. Directional topographic site response at Tarzana observed in aftershocks of the 1994 Northridge, California, earthquake: implications for mainshock motions. Bull. Seismol. Soc. Am. 86, 193–208.
Stolte, A.C., Cox, B.R., Lee, R.C., 2017. An experimental topographic amplification study at Los Alamos National Laboratory using ambient vibrations. Bull. Seismol. Soc. Am. 107 (3), 1386–1401.
University of Innsbruck, WSL/SLF Davos, 2015. Matterhorn Cryosphere Observatory, Switzerland. ETH Zurich.
Weber, S., Fäh, D., Beutel, J., Faillettaz, J., Gruber, S., Vieli, A., 2018. Ambient seismic vibrations in steep bedrock permafrost used to infer variations of ice-fill in fractures. Earth Planet. Sci. Lett. 501, 119–127.
Weber, S., Beutel, J., Da Forno, R., Geiger, A., Gruber, S., Gsell, T., Hasler, A., Keller, M., Lim, R., Limpach, P., Meyer, M., 2019. A decade of detailed observations (2008–2018) in steep bedrock permafrost at the Matterhorn Hörnligrat (Zermatt, CH). Earth Syst. Sci. Data 11, 1203–1237.